Dalton Transactions

ROYAL SOCIETY OF CHEMISTRY

COMMUNICATION

View Article Online
View Journal | View Issue

Check for updates

Cite this: *Dalton Trans.*, 2023, **52**, 4303

Received 15th February 2023,
Accepted 15th March 2023

DOI: 10.1039/d3dt00479a

rsc.li/dalton

Mechanistic insight into Pb^{2+} and Hg^{2+} ion sensing using cobalt-based coordination polymer in aqueous phase†

Akashdeep Nath, Diti Vikram Gaikwad and Sukhendu Mandal *

Emissive inorganic–organic hybrid materials open up a new prospect of fast and efficient heavy metal ion sensing in an aqueous medium. Here, we demonstrate highly sensitive lead(II) ion detection attributed to excited-state host–guest interaction, where mercury(II) shows lesser quenching efficiency due to both ground- and excited-state interaction.

The industrial revolution and human activities have escalated the direct production of hazardous wastes like heavy metals, which mix with groundwater to cause an adverse effect on the Earth's ecosystem.[1,2] Lead, one of the most toxic metal ion contaminants, causes severe life-threatening problems like neurological and renal disorders and delayed development upon exposure to even low ion concentrations.[3,4] Thus, detecting Pb(II) ions at ppm or sub-ppm level in water is highly necessary for environmental sustainability. The detection of Pb(II) ions in water relies mainly on atomic absorption/emission spectroscopy, inductive coupled plasma-optical emission spectroscopy (ICP-OES), ICP-MS, XRF spectroscopy, *etc.*[5–8] However, their high cost and time-consuming methods impede their processibility in common laboratories. Thus, rapid, remote, highly efficient Pb(II) ion detection in water has faced a substantial challenge for real-time applications. In this regard, a luminescent probe could be a promising material for its quick, easy, cost-effective accessibility as a metal ion sensor.[9,10] Luminescent inorganic–organic hybrid materials, like coordination polymers, offer the prospect of overcoming this challenging problem.

Coordination polymers (CPs) are constructed from metal centers and organic linkers, resulting in a highly crystalline framework material.[11,12] Numerous choices of metal nodes, organic linkers, and their several orientation patterns make the CPs tunable and versatile in structural and functional aspects. This tailor-made material attains its luminescence by utilizing a π-electron-rich organic linker.[13] The interaction between the organic linker and analyte perturbs the emission property of the overall material and thus acts as a sensor probe. Several luminescent frameworks have been reported in the sensing of metal ions, oxyanions, and organic pollutants;[14–16] though the literature reports for lead ion sensing are not substantial (Table S1†). The sensing of the Pb(II) ion in framework materials is mainly reported as a ground-state interaction between Pb(II) and oxygen from organic linkers.[13,17–19] However, the excited-state host–guest interaction in Pb(II) ion sensing is elusive, and the molecular-level understanding of excited-state interaction is largely untapped. Herein, we synthesize a new emissive cobalt-based coordination polymer, $[Co(BTB)(4,4'\text{-azopyridine})]\cdot H_2O\cdot DMF$, **1**, containing 1,3,5-tris(4-carboxyphenyl)benzene (BTB) and 4,4′-azopyridine as organic linkers, which demonstrates "turn-off" lead(II) ion sensing in water with a limit of detection (LOD) of $7.082\ (\pm 0.08) \times 10^{-8}$ M (0.0147 ppm) Pb(II) ions. Spectroscopic data reveals the host–guest interaction to be an excited-state phenomenon. In a comparative study, we elucidated the lower quenching efficiency for mercury(II) ions than for lead(II) ions.

Solvothermal synthesis of cobalt nitrate along with two co-linkers, 4,4′-azopyridine and BTB in a 7 : 3 H_2O : DMF mixture at 100 °C, yields orange-colored plate-like crystals of **1**. It was crystallized in a triclinic crystal system with space group $P\bar{1}$ (2) obtained from single-crystal X-ray diffraction measurement (Fig. 1; for crystallographic details, selected bond lengths, and bond angles, see Tables S2–S4†). The asymmetric unit contains one cobalt center, one 4,4′-azopyridine, and one BTB linker, along with one water molecule and a fragmented DMF molecule (Fig. S1†). The structural scaffold contains one crystallographically unique, slightly distorted octahedral cobalt center (Fig. S2†), where four equatorial coordination positions are occupied by three different BTB linkers and two axial positions by two 4,4′-azopyridine molecules (with Co–N bond distances

School of Chemistry, Indian Institute of Science Education and Research Thiruvananthapuram, Thiruvananthapuram, Kerala-695551, India.
E-mail: sukhendu@iisertvm.ac.in

†Electronic supplementary information (ESI) available. CCDC 2238686. For ESI and crystallographic data in CIF or other electronic format see DOI: https://doi.org/10.1039/d3dt00479a

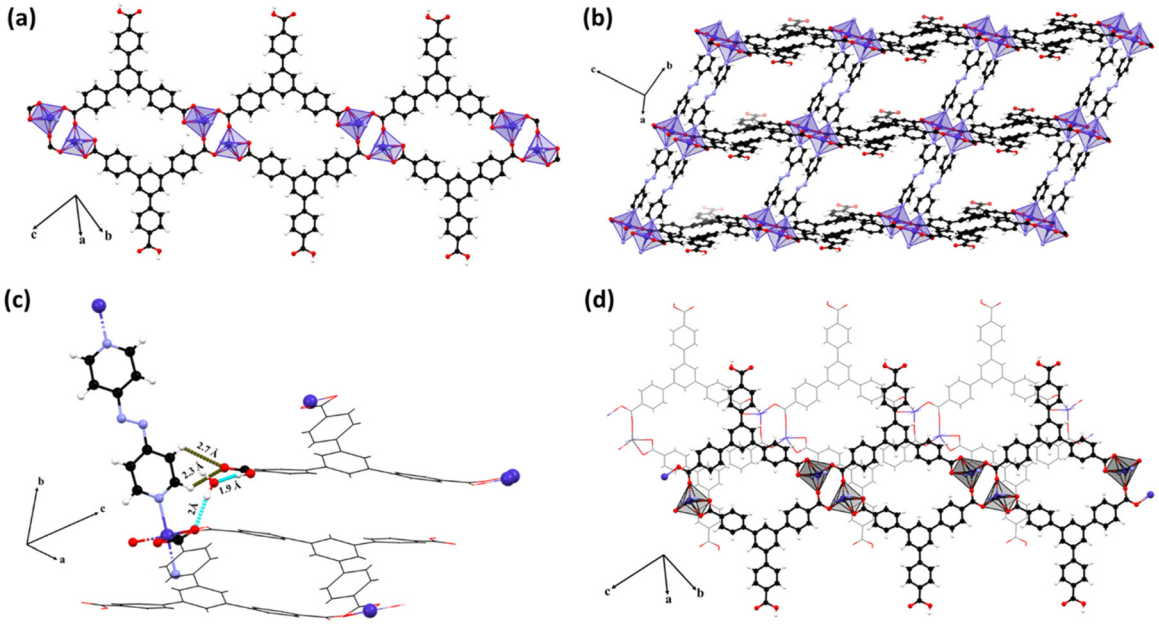

Fig. 1 (a) One-dimensional chain containing cobalt centers and BTB linkers, (b) two-dimensional pillar-layered structure, (c) crystal packing showing strong inter-molecular hydrogen bonding between two-dimensional layered structures, (d) intercatenated layered framework.

of 2.1–2.2 Å). The BTB molecules are coordinated to the metal center in two different fashions, *i.e.*, (a) μ_1-η^1:η^1 mode with Co–O bond distances of 2.1 and 2.4 Å, (b) μ_2-η^1:η^1 mode with the same Co–O bond distances of 2 Å; whereas the third carboxylic end of BTB is presented as its protonated form (Fig. S3†). The BTB linkers, along with cobalt centers, form a one-dimensional chain (Fig. 1a), which is pillared by the two cofacially arranged 4,4′-azopyridine with an inter-ligand distance of 3.9 Å to form a two-dimensional layered structure (Fig. 1b). Crystal packing shows that the two-dimensional layered structures are strongly coordinated with inter-linkers and solvated water-mediated hydrogen bonding (of distances 2–2.7 Å) (Fig. 1c). The protonated carboxylate end of BTB from one layer forms a hydrogen bond with the 4,4′-azopyridine molecule of another layer, while the solvated water molecule forms hydrogen bonds between two BTB linkers from different layers, producing an intercatenated layered structural scaffold (Fig. 1d). Topological analysis revealed that the framework possesses a 6-c uninodal net, with a Schläfli symbol of $\{3^3{\cdot}4^{10}{\cdot}5.6\}$ (see ESI†).[20] The FT-IR spectra (Fig. S4†) confirm the structural description obtained from Sc-XRD, where $\nu_{stretch}$ (–C═O) and $\nu_{stretch}$ (–C–O–) are shifted from 1690 cm^{-1} to 1710 cm^{-1} and from 1110 cm^{-1} to 1105 cm^{-1} from free BTB to BTB incorporated in **1**. The $\nu_{stretch}$ (–C═N–) and $\nu_{stretch}$ (–C–N–) of 4,4′-azopyridine are shifted from 1570 cm^{-1} to 1542 cm^{-1} and from 1413 cm^{-1} to 1409 cm^{-1}, respectively, in **1** compared to the free ligand. A broad $\nu_{stretch}$ (–OH) is observed in both free BTB and **1** centered at *ca.* 3000 cm^{-1}. The powder XRD pattern shows the phase purity of the compound compared with the simulated one (Fig. S5†). In thermogravimetric analysis, CP shows an initial 6% weight loss at *ca.* 100 °C due to the removal of solvated water and DMF molecules (Fig. S6a†). The CP is thermally stable up to 295 °C. After that, the pristine framework destructs to form Co_3O_4 (as confirmed by PXRD, Fig. S6b†).

Steady-state spectroscopy shows an absorption maximum at 275 nm for the BTB linker in water (Fig. S7†). The time-dependent density of states (TD-DFT) calculation of optimized BTB reveals that the absorption peak corresponds to HOMO (highest occupied molecular orbital)−1 → LUMO (lowest unoccupied molecular orbital) ($\pi \rightarrow \pi^*$) and HOMO−1 → LUMO+1 electronic transitions ($\pi \rightarrow \pi^*$). 4,4′-Azopyridine shows a primary absorption peak at 282 nm with a small peak at 450 nm (Fig. S8†). TD-DFT reveals a HOMO−1 → LUMO electronic transition ($\pi \rightarrow \pi^*$) of the stable *trans*-oriented 4,4′-azopyridine molecule at 282 nm, whereas a small peak at 450 nm arises from the HOMO → LUMO electronic transition ($n \rightarrow \pi^*$) of the higher-energized *cis*-orientation. We surmise that a small amount of *cis*-form is generated from its stable *trans*-form upon light absorption. The absorption spectrum of **1** contains both 4,4′-azopyridine and BTB ranges, with a maximum at 275 nm (Fig. S9†).

The luminescence of both linkers and **1** was measured in water. BTB exhibits an emission maximum at 362 nm (Fig. S10†), whereas 4,4′-azopyridine is non-emissive. The emission maximum of **1** was obtained at 357 nm, attributed to BTB linkers (Fig. 2a and S11†). The excitation spectra of both BTB and **1** were found to be 275 nm when considering their respective emission maxima (Fig. S12†). The quantum yield (QY) of **1** was found to be 0.22, whereas it was 0.20 for the BTB linker. The 10% increase in QY can be accounted for by the slight rigidification of the BTB linker from the two carboxylate

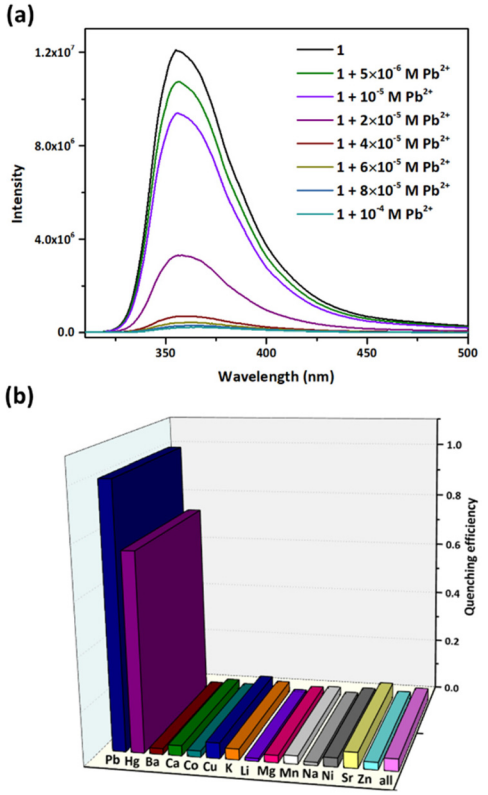

Fig. 2 (a) "Turn-off" fluorescence Pb(II) ion sensing, (b) bar diagram showing higher Pb sensing efficiency on a relative scale.

ends, as well as enhanced repulsion between the hydrogen atoms of adjacent phenyl moieties resulting in a decrease in thermal motion.[21,22] The lifetime decay profiles of BTB and **1** also reflect similar conclusions to those drawn from the QY value comparison (Fig. S13 and Tables S5, S6†). BTB shows two-component decay (τ_1 = 5 ns, α_1 = 0.19, τ_2 = 21 ns, α_2 = 0.81). The 19% fast population decay can be attributed to aggregation-induced emission quenching,[23] whereas its primary component (81%) shows a higher lifetime of 21 ns. The fluorescence decay (two components; τ_1 = 6 ns, α_1 = 0.02; τ_2 = 23 ns, α_2 = 0.98) of **1** reflects the small structural rigidification of BTB after impregnation into **1**. The framework structure allows BTB molecules to have a considerable separation (~4 Å) to reduce the extent of inter-molecular aggregation in the excited state, thus showing reduced fast decay (due to aggregation) from 19% to 2% compared to its pristine state.

Due to its natural high luminescence and stability in water (Fig. S14†), we utilized **1** to sense toxic heavy metal ions, like Pb(II), in water. For sensing studies, a uniformly dispersed **1** solution (water) was used. The uniform dispersity of the considered **1** solution was examined through the Tyndall effect, observing no sparkling of a laser beam (532 nm) at 0 min and also after 1 h (Fig. S15†).[9] Moreover, dynamic light scattering (DLS) shows that the particles are mono-dispersed with an average diameter of 219 nm (Fig. S16†). We performed fluorescence sensing of various concentrations of Pb(II) ions in water, which shows "turn-off" fluorescence quenching from the pristine emission (Fig. 2a). A linear fit obtained from the emission quenching ratio *vs.* Pb(II) ion concentration, followed by utilization of eqn (S2) and (S3)† gave its LOD as 7.082 (±0.08) × 10^{-8} M Pb(II) ions (0.0147 ppm) from an average of 5 measurements, which meets the maximum allowed level (0.015 ppm) of lead in drinking water set by the U.S. Environmental Protection Agency[24] (Fig. S17;† for a comparative study, see Table S1†). We carried out comparative sensing studies with different monovalent and bivalent metal ions (Li^+, Na^+, K^+, Mg^{2+}, Ca^{2+}, Sr^{2+}, Ba^{2+}, Mn^{2+}, Co^{2+}, Cu^{2+}, Ni^{2+}, Zn^{2+}, Hg^{2+} and also a mixture of all these metal ions except Hg^{2+}) under similar conditions (10^{-5} M). We plotted the emission quenching for these metal ions on a comparative scale, taking the emission quenching as unity when Pb(II) ions are added in the presence of individual metal ions (Fig. 2b), depicting the high selectivity of **1** towards Pb(II) ions in water. The structural stability of **1** was retained before and after Pb(II) ion sensing, as depicted from PXRD (Fig. S18†). The utility of a sensing probe relies on its reversibility and recyclability. We washed **1** thoroughly with water after Pb(II) ion sensing and again recycled it. Fig. S19† shows the retention of **1** emission and quenching efficiency even after seven consecutive cycles, showing its high recyclability. Compound **1** shows similar Pb(II) ion sensing over a broad pH range from pH 4 to 9 (Fig. S20†). We also carried out Pb(II) sensing by **1** in different waters from various environmental sources, like tap water, river water, and drinking water, with the same methodology as for distilled water. Table S7† shows similar Pb(II) ion detection efficacy in natural water sources to distilled water, which is desirable for practical applications.

To determine a plausible probe–analyte mechanism, we carried out the UV-Vis absorption spectra of **1** upon adding different concentrations of Pb(II), which showed no shift in absorption maximum and no extra absorption peak

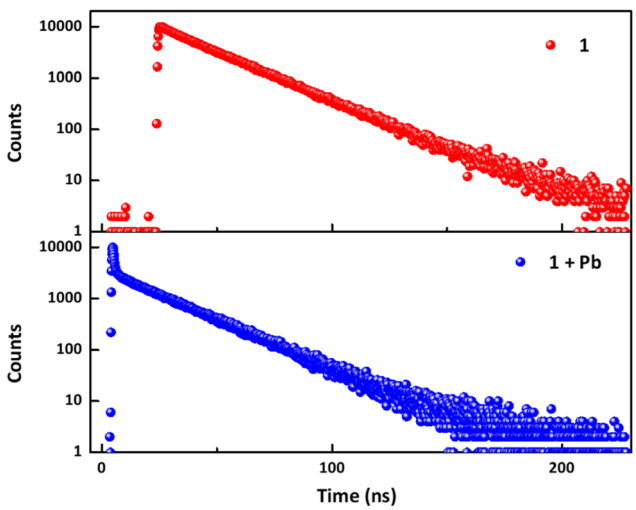

Fig. 3 Fluoresce decay profile of **1** in water and **1** after adding $PbCl_2$ solution (λ_{ex} = 310 nm; λ_{probe} = 357 nm).

(Fig. S21†). This reveals that the probe–analyte interaction does not occur in the ground state. We further studied the lifetime decay profile of **1** after Pb(II) ion addition. Fig. 3 shows a sharp change in the fluorescence decay profile, where three-component decay (τ_1 = 0.5, τ_2 = 6 ns, τ_3 = 23 ns) was observed for **1** after adding Pb(II) ions (Table S8†), whereas **1** shows two-component decay (τ_1 = 6 ns, τ_2 = 23 ns) arising from BTB linkers. A sharp lifetime decay of 0.5 ns is attributed to host–guest interaction in the excited state. We plotted the emission intensity ratio of **1** with different Pb(II) ion concentrations and subsequently utilized the Stern–Volmer (SV) equation to get Stern–Volmer constants of 2.2×10^4 M^{-1} (at 40 °C) and 3.8×10^4 M^{-1} (at 50 °C) with a linear fit (R^2 = 0.999 and 0.999, respectively) (Fig. S22†). The increased SV constants with increasing temperature realize the dynamic (or collision) quenching mechanism between **1** and Pb(II) ions. As dynamic quenching depends on the number of host–guest collisions, increases in temperature result in more collisions and, thus, a higher SV slope.[25]

In search of mechanistic details about host–guest interaction in the excited state, a DFT calculation was carried out to obtain the HOMO and LUMO energy levels. As BTB is solely responsible for the emission of **1**, we concentrated on the energy levels of the BTB linker and $PbCl_2$ after ground-state optimization and using the PCM model for water. Fig. 4 shows the energy levels, where the LUMO of $PbCl_2$ (−0.74 eV) lies between the HOMO (−8.54 eV) and LUMO (−0.14 eV) of the BTB linker, which enables electron transfer from the LUMO of excited BTB to the LUMO of $PbCl_2$, suggesting photo-induced electron transfer (PET) as a plausible mechanism.[26]

These orbital energy levels also reveal the reason behind the "turn-off" emission quenching of **1** in the presence of Pb(II) ions. The "turn-off" quenching of the fluorescence probe happens when the LUMO of the analytes lies between the HOMO and LUMO of the probe, which facilitates another relaxation pathway of the excited host molecule from its own LUMO to the LUMO of the analyte molecule, rendering an overall decrease in fluorescence efficiency of the fluorescence probe.[27] The mid-gap-positioned LUMO of $PbCl_2$ in between the HOMO and LUMO of the BTB linker facilitates a bypass relaxation pathway for excited BTB linkers and thus shows "turn-off" quenching.

Generally, weak interactions like dipole–dipole interaction and lone-pair–π interaction will initiate this excited-state host–guest interaction.[28] We calculated the dipole moment of $PbCl_2$ in water using DFT, which was found to be high (6.9 D) as it is a bend-in structure (note that the dipole moment of BTB was 4.36 D). Moreover, both Pb and Cl contain a lone-pair, which can interact with phenyl moieties (lone-pair–π interaction). To find the extent of stabilization due to host–guest interaction, we extracted the optimized S_1 geometry of the BTB molecule, froze all the coordinates (except hydrogen atoms), and allowed $PbCl_2$ to move to find its most stable position near the BTB molecule. After obtaining energy minima of such a BTB–$PbCl_2$ adduct (where the average distance between BTB–$PbCl_2$ is *ca.* 3 Å), we calculated its stabilization energy of 0.6 eV with respect to its counterparts using eqn (S4)† (Fig. 5a). The molecular orbital diagram of the BTB–$PbCl_2$ adduct shows a HOMO, which is localized over BTB and $PbCl_2$ molecules, whereas these are delocalized in the LUMO, which reveals higher interaction in the excited state than in their ground state. Note that the energy difference between the LUMOs of BTB and $PbCl_2$ is also lower (ΔE = 0.6 eV) than their HOMOs (ΔE = 1.2 eV) to facilitate better orbital overlap in their LUMOs, resulting in excited-state host–guest interaction instead of ground-state interaction. We also optimized other possible orientations of $PbCl_2$ over the BTB molecule, which also engendered similar stabilization energies and MOs to the above (Fig. S23–S27 and Table S9†).

In a comparative study, we observed turn-off emission in the case of Hg ions, but the efficiency was less compared to the Pb ions. We calculated the LOD of Hg(II) ions, which was found to be lower (9.048×10^{-8} M or 0.018 ppm) than for Pb

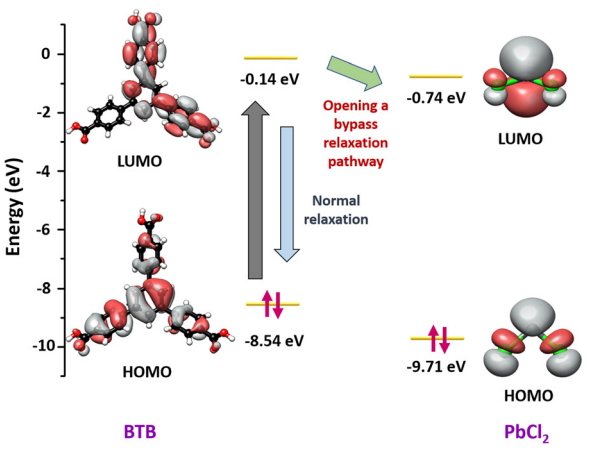

Fig. 4 Pictorial representation of energy levels of BTB and $PbCl_2$ and showing an alternative relaxation pathway.

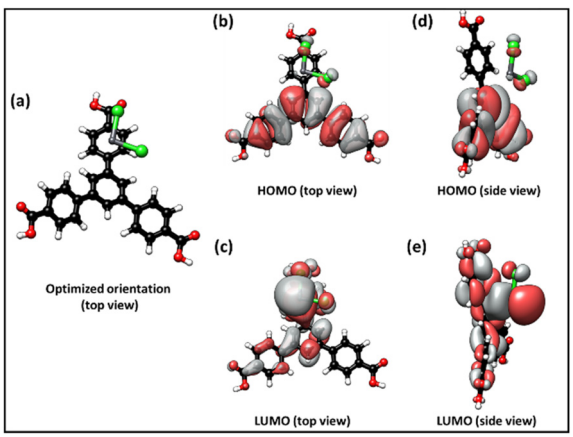

Fig. 5 (a) Optimized $PbCl_2$ position on the BTB molecule, their corresponding HOMO (b: top view, c: side view) and LUMO (d: top view, e: side view).

ions (Fig. S28†). Moreover, we show the selective Hg sensing and also the higher anti-inference ability for Pb(II) sensing than Hg(II) ions in the presence of mixed metal ion solution in Fig. S29.† The bar diagram was plotted by considering the emission quenching as unity when Pb(II) ions are added. A mixed-metal ion solution shows only 4% emission quenching, whereas Hg(II) ions can quench 71% of the initial emission in the presence of mixed-metal ions. The Pb(II) ions can further quench emission intensity by 29% in the presence of all metal ion mixtures, including Hg(II). We investigated this lower emission quenching for $HgCl_2$ than $PbCl_2$. The absorption spectra of **1** after adding different concentrations of Hg(II) ion solution show a red-shift (Fig. S30†), suggesting a ground-state interaction between host and $HgCl_2$ molecules. XPS measurements of **1** were carried out before and after the addition of Hg(II) ion solution to determine the interacting atoms between the probe and analytes. The XPS spectra of **1** show all the characteristic peaks of the pristine material (Fig. S31†). The Co 2p spectrum shows both the characteristic $2p_{3/2}$ and $2p_{1/2}$ peaks (also their satellite peaks). The deconvoluted O 1s spectra show peaks at ~530.96 eV (Co–O) and ~532.84 eV (C═O). The N 1s spectra contain a broad peak at ~400 eV, which is deconvoluted into two peaks at ~399.47 eV and ~400.67 eV coming from pyridine-N and azo-N. The XPS spectra of **1** after adding Hg(II) show characteristic Hg $4f_{7/2}$ and $4f_{5/2}$ peaks at ~102.16 eV and ~106 eV, respectively (Fig. S32†). The XPS spectra of C 1s, Co 2p, and O 1s remain almost the same as those in a pristine state. In contrast, N 1s shows one new peak at ~403.9 eV along with existing pyridine-N and azo-N peaks, indicating an interaction between Hg(II) ions and the –N═N– group.[10] This interaction is favorable due to soft-acid (Hg^{2+}) and soft-base (azo-N) interaction. In a comparative study, the XPS spectra of **1** before and after the addition of Pb(II) ion solution remained unchanged, indicating no ground-state interaction between Pb (II) ions and **1** (Fig. S33†). Moreover, the lifetime decay profile of **1** after adding Hg(II) ions (Fig. S34 and Table S10†) shows a new fast decay (τ_1 = 0.3 ns) component along with two existing decay profiles (τ_2 = 22 ns, τ_3 = 6 ns) like its pristine state. The fast decay of 0.3 ns suggests that Hg(II) ions also interact with **1** in the excited state. All these experimental data revealed that both ground-state and excited-state host–guest interactions are responsible for the emission quenching of **1** in the case of Hg (II) addition.

In the case of Pb(II) ions, they solely interact with BTB linkers of **1** in the excited state, whereas Hg(II) ions interact both with BTB linkers of **1** in the excited state and 4,4′-azopyridine of **1** in ground state. As Hg(II) ions can interact with both linkers, the population of Hg(II) ions interacting with BTB will be lower than in the Pb(II) case. As the emission of **1** is solely the responsibility of BTB linkers (4,4′-azopyridine is non-emissive), the quenching efficiency will be lower for Hg(II) than for Pb(II) ions. Note that the amplitude of fast component decay (α_1) is higher for Pb(II) (0.1) addition than for Hg(II) (0.06) (Tables S8 and S10†), which indicates the greater extent of excited-state interaction in the case of $PbCl_2$ addition than $HgCl_2$.

Conclusions

In summary, we synthesized a new cobalt-based emissive CP, which shows "turn-off" emission sensing with an LOD of 7.082 (±0.08) × 10^{-8} M (0.0147 ppm) Pb(II) in water. The host–guest interaction was found to be an excited-state interaction. Quantum chemical calculation shows lower ΔE between the LUMOs of host and guest molecules, favoring an excited-state interaction. Moreover, the LUMO position of $PbCl_2$ explains the "turn-off" emission quenching mechanism. This coordination polymer is able to sense Pb(II) ions over a wide range of pH from 4 to 9, as well as in various natural waters for practical applications. Finally, we demonstrate the dual types of **1**-$HgCl_2$ interactions (both ground and excited state), which result in a lower emission quenching than for $PbCl_2$ addition.

Author contributions

The work was conceived by A. N. and S. M. All the works were done by A. N. and D. V. G. Both A. N. and S. M. analyzed the results and wrote the manuscript. S. M. supervised the research work. The manuscript has been approved by all the authors.

Conflicts of interest

There are no conflicts to declare.

Acknowledgements

We thank Prof. Di Sun (Shandong University) for the Sc-XRD facility. We thank the support for high-performance computing time at the Padmanabha cluster, IISER Thiruvananthapuram, India.

Notes and references

1 S. Bolisetty, M. Peydayesh and R. Mezzenga, *Chem. Soc. Rev.*, 2019, **48**, 463–487.
2 P. Amoatey and M. S. Baawain, *Water Environ. Res.*, 2019, **91**, 1272–1287.
3 J. E. Johnston, M. Franklin, H. Roh, C. Austin and M. Arora, *Environ. Sci. Technol.*, 2019, **53**, 6000–6006.
4 H. Needleman, *Annu. Rev. Med.*, 2004, **55**, 209–222.
5 C. Duran, H. B. Senturk, L. Elci, M. Soylak and M. Tufekci, *J. Hazard. Mater.*, 2009, **162**, 292–299.
6 E. L. Silva, P. dos Santos Roldan and M. F. Giné, *J. Hazard. Mater.*, 2009, **171**, 1133–1138.
7 J. Yin, Z. Jiang, G. Chang and B. Hu, *Anal. Chim. Acta*, 2005, **540**, 333–339.
8 B. Zawisza and R. Sitko, *Spectrochim. Acta, Part B*, 2007, **62**, 1147–1152.

9 A. Nath, G. M. Thomas, S. Hans, S. R. Vennapusa and S. Mandal, *Inorg. Chem.*, 2022, **61**, 2227–2233.
10 A. Pankajakshan, D. Kuznetsov and S. Mandal, *Inorg. Chem.*, 2019, **58**, 1377–1381.
11 S. Kitagawa, R. Kitaura and S. Noro, *Angew. Chem., Int. Ed.*, 2004, **43**, 2334–2375.
12 S. Kitagawa and R. Matsuda, *Coord. Chem. Rev.*, 2007, **251**, 2490–2509.
13 X. An, Q. Tan, S. Pan, H. Liu and X. Hu, *Spectrochim. Acta, Part A*, 2021, **247**, 119073.
14 M. Marimuthu, S. S. Arumugam, D. Sabarinathan, H. Li and Q. Chen, *Trends Food Sci. Technol.*, 2021, **116**, 1002–1028.
15 X. Fang, B. Zong and S. Mao, *Nano-Micro Lett.*, 2018, **10**, 64.
16 J. Yang, W. Ni, B. Ruan, L.-C. Tsai, N. Ma, D. Shi, T. Jiang and F.-C. Tsai, *ECS J. Solid State Sci. Technol.*, 2021, **10**, 56003.
17 G. Ji, J. Liu, X. Gao, W. Sun, J. Wang, S. Zhao and Z. Liu, *J. Mater. Chem. A*, 2017, **5**, 10200–10205.
18 A. H. Gore, D. B. Gunjal, M. R. Kokate, V. Sudarsan, P. V. Anbhule, S. R. Patil and G. B. Kolekar, *ACS Appl. Mater. Interfaces*, 2012, **4**, 5217–5226.
19 S. Xu, L. Zhan, C. Hong, X. Chen, X. Chen and M. Oyama, *Sens. Actuators, B*, 2020, **308**, 127733.
20 V. A. Blatov and D. M. Proserpio, *Acta Crystallogr., Sect. A: Found. Crystallogr.*, 2009, **65**, 202–212.
21 Z. Wei, Z.-Y. Gu, R. K. Arvapally, Y.-P. Chen, R. N. J. McDougald, J. F. Ivy, A. A. Yakovenko, D. Feng, M. A. Omary and H.-C. Zhou, *J. Am. Chem. Soc.*, 2014, **136**, 8269–8276.
22 The average dihedral angle between adjacent phenyl rings is lesser (*ca.* 26°) inside the framework compared to the free molecule (*ca.* 42°), resulting in steric repulsion between hydrogen atoms of adjacent phenyl rings.
23 S. Banerjee, A. K. Both and M. Sarkar, *ACS Omega*, 2018, **3**, 15709–15724.
24 Z. Li, Z. Zhan and M. Hu, *CrystEngComm*, 2020, **22**, 6727–6737.
25 J. R. Lakowicz, *Principles of Fluorescence Spectroscopy*, Springer, New York, 3rd edn, 2006.
26 M. Formica, V. Fusi, L. Giorgi and M. Micheloni, *Coord. Chem. Rev.*, 2012, **256**, 170–192.
27 B. Gole, A. K. Bar and P. S. Mukherjee, *Chem. – Eur. J.*, 2014, **20**, 2276–2291.
28 K. S. Asha, K. Bhattacharyya and S. Mandal, *J. Mater. Chem. C*, 2014, **2**, 10073–10081.

